Journal of CO2 Utilization 74 (2023) 102536

Contents lists available at ScienceDirect

Journal of CO2 Utilization

journal homepage: www.elsevier.com/locate/jcou

A sustainable methodology to produce open-cell porous membranes with control on the dense layer thickness

D. Cuadra-Rodríguez [a,*], C. Soto [b,c], F.J. Carmona [b,c], A. Tena [b,c], L. Palacio [b,c], M.A. Rodríguez-Pérez [a,d], J. Pinto [a,d,e]

[a] Cellular Materials Laboratory (CellMat), Condensed Matter Physics Department, University of Valladolid, Paseo Belén 7, 47011 Valladolid, Spain
[b] Surfaces and Porous Materials (SMAP), Associated Research Unit to CSIC. University of Valladolid, Facultad de Ciencias, Paseo Belén 7, 47011 Valladolid, Spain
[c] Institute of Sustainable Processes (ISP), University of Valladolid, 47011 Valladolid, Spain
[d] BioEcoUVA Research Institute on Bioeconomy, University of Valladolid, 47011 Valladolid, Spain
[e] Archaeological and Historical Materials (AHMAT) Research Group, University of Valladolid, Paseo de Belén 7, 47011 Valladolid, Spain

ARTICLE INFO

Keywords:
Gas separation
Permeance
Open-Cell nanostructures
Gas barrier approach
Skinless nanocellular foams

ABSTRACT

A new approach to produce porous membranes with dense or porous top layer is proposed in this work by employing a solvent-free method. PMMA/MAM formulations were selected as a base material in order to create open-cell or close-cell structures by gas dissolution foaming employing CO_2 as a blowing agent. Furthermore, by introducing the gas diffusion barrier approach to CO_2 dissolution foaming, it is possible to control the thickness of the dense layer in both edges, obtaining defect-free membranes (i.e., completely dense without pin-holes). The effectiveness of nanocellular polymers as gas separation membranes was evaluated. In this way, the permeability, selectivity, and permeance were correlated to the cellular structure (open or close-cell) as well as to the dense layer thickness. Furthermore, the effective thickness of the selective layer has been calculated from gas permeability measurements, obtaining an accurate control of that parameter from the tunable cellular structure. Therefore, membranes composed of desired selective layer and a porous structure as a mechanical support are produced by a solvent-free methodology.

1. Introduction

The industry is unstoppable evolving towards more sustainable processes. Ideally, the new methodologies will keep or even enhance the competitiveness of the process by improving the material properties and reducing their footprint [1]. Some industrial processes (e.g., fabrication, energy consumption, transport…) involve the use or generation of some pollutants such as mixes of gases, which, instead of being released to the atmosphere, should be disaggregated and stored properly for further using [2,3]. Membranes can remove selectively an undesired element, i.e., from the emitting source, preventing the emission of this component. In fact, gas separation membranes are widely employed for capturing or isolating a single gas from a mixture. Although the gas separation technique was discovered in the early 19th century, the first generation of membranes were not fabricated by the industry with that specific purpose until several decades ago [4–9].

Traditionally, gas separation performances are evaluated as thick dense films with thicknesses around 50–150 μm. Their performance for the separation of a specific gas mixture is evaluated by the relationship between their permeability and selectivity according to the upper bond stablished by Robeson in 1991 [10]. However, the permeance (gas flux), rather than permeability, has pointed out as more highlighted property in industrial scenarios with the aim of raising the real gas flux through the membrane without losing selectivity [11–13]. In this case, the membranes are generally formed by very thin selective layer, 0.3–0.5 μm, placed on top of porous supports which provide mechanical strength. Therefore, the two main possibilities in the development of gas separation membranes are: the designing of composite membranes (i.e., several layers with different properties, function, and porosity); thin film composites with a thin defect-free film as a selective layer on top of a porous strong substrate as a mechanical support [2,4,14]; or the formation of asymmetric membranes where the porous substrate and the dense layer are formed by the same material in a single step.

The production of thinner membranes, especially in the selective layer (or layers), leaves several advantages such as the reduction of the material and production costs, or the increase in permeance for

* Corresponding author.
E-mail address: dcuadra@fmc.uva.es (D. Cuadra-Rodríguez).

https://doi.org/10.1016/j.jcou.2023.102536
Received 26 April 2023; Received in revised form 28 June 2023; Accepted 1 July 2023
Available online 5 July 2023

enhancing the effectiveness of the membranes in industrial processes [11,15]. Most of these techniques are based on reducing the membrane thickness [16,17], functionalizing some layers [18], or taking benefit of the CO_2-philicity [19–22] to enhance the permeance through the membrane.

Despite the interesting advantages offered by multilayer composites and thin film membranes, the fabrication of extremely thin dense layers (0.1–0.5 μm) presents some difficulties such as, the presence of defects, the complexity of the process by assembling several layers, or the use of hazardous solvents in the fabrication techniques [2,23]. Some processes, such as extrusion, may lead to the generation of defects which is very challenging in the case of very thin selective layers [24,25]. Over the time, this situation changes due to the rearrangement of the polymer chains approaching to a more thermodynamically stable state [4,23,26]. On the other hand, the production of thin film composites includes complicated and non-green techniques which involve hazardous solvents to place the different layers [27,28].

From this overview, the main challenge in the fabrication of membranes for gas separation applications is to produce integral asymmetric membranes with a thin dense layer together with a bulk porous structure in a single, straightforward, and solvent-free methodology. Following these requirements, a potential solution could be reached using cellular polymers, which are lightweight materials composed of both gas and solid phases with cell sizes from hundreds of microns to tens of nanometers [29–31]. In particular, cellular structures produced by gas dissolution foaming, a physical gas dissolution without involving harmful pollutants, can be created from a wide range of polymers and easily tuned by the foaming parameters. Their morphology shows a symmetric cellular structure in a sandwich-like form: a homogenous cellular structure in the centre which represent the major of the sample and dense skins in the borders with thicknesses around tens to hundreds of microns [32,33]. This kind of structures could perform as gas separation membranes, acting the dense skin as a selective layer and the cellular core as a strong mechanical support. However, some challenges such as the large thickness of the dense skins, the cell interconnectivity, or the impossibility of foaming thin films have been hindering the extensive application of cellular polymers in gas separation. In our recent work, those limitations have been overcome allowing the control of the dense skin thickness and enabling the foaming in thin films by employing the gas barrier approach [34]. This technique consists of keeping as much CO_2 concentration as possible into the polymeric structure at the foaming time by employing a gas diffusion barrier on the top and/or bottom sides of the film. Furthermore, thin films and micrometric fibres were foamed for first time by employing the same approach, obtaining homogenous cellular structures similar to bulk pieces and hollow fibres, respectively [34,35].

On the other hand, different strategies developed in gas dissolution foaming enabled to interconnect the cells creating an open-cell structure. For instance, Pinto et al. [36] produced open-cell nanocellular structures from block copolymer nanocomposites (PMMA/MAM) by gas dissolution foaming based on the heterogenous nucleation approach [37–39]. PMMA/MAM presented good foamability properties achieving cell interconnection in the inner cellular structure. Nevertheless, the huge thickness of the dense skins in the edges hindered in that moment their use in applications such as filtration or gas separation.

Therefore, the interconnection between the inner cellular structure and the external medium, and the control on the thickness of the dense skins could allow their application as gas separation membranes. In this work, this new methodology has been used to obtain gas permeation membranes fabricated by solvent-free techniques. By the gas barrier approach, it was possible to modify the selective layer thickness. In all the cases, a porous structure, acting as a mechanical support, was obtained. Then, this solvent-free approach allows to form a selective layer supported in an open porous structure by using a CO_2 foaming process in a single step. Porous PMMA/MAM composites were produced from two different compositions and the permeability properties were studied by time-lag measurements using several gases (e.g., helium, nitrogen, oxygen, methane, and carbon dioxide). The gas permeance was analysed as a function of the porous structure and the presence (or not) of the dense selective layer.

2. Experimental section

2.1. Materials

Two different formulations of poly(methyl methacrylate) (PMMA) and methyl methacrylate-b–butyl acrylate-b–methyl methacrylate (MAM) triblock copolymer were selected for producing the PMMA/MAM blends. PMMA V825T (VT), MAM M42, and MAM M53 were purchased from ARKEMA company (Colombes, France), while PMMA 8N were purchased from EVONIK (Darmstadt, Germany). The main characteristics of the PMMAs and MAMs such as the thermal properties, the molecular weight, the poly(butyl acrylate) (PBA) content, among other can be found in the Supporting Information (Section S1, Table S1).

On the other hand, poly(vinyl alcohol) (PVOH) MOWIFLEX C17, purchased from Kuraray Europe (Hattersheim am Main, Deutschland), was employed as a gas diffusion barrier on the polymer surfaces according to the PVOH technique [34]. Besides, a medical grade of CO_2 (99.9% purity) was employed as a blowing agent for foaming experiments. After the foaming process, deionized water was employed to remove the PVOH from the surfaces of the membranes.

2.2. Fabrication of the membranes

The compositions of PMMA/MAM employed were selected according to the expected cellular structures (open- and close-cell). Following this criterion, polymer structures resulting in open-cell nanostructures (VT/M42) and close-cell microstructures (8N/M53) [40]. Both formulations, VT/M42 and 8N/M53, were mixed in 15/85 wt content and dissolved in chloroform at 10 wt%. Afterwards, the solid films fabricated by the solvent casting method were cut in 3×3 cm^2 pieces with thicknesses around 400 μm. Table 1 shows the PMMA/MAM films used as solid precursors to fabricate porous membranes (labelled as 'films' from now on). In addition, the external surfaces of the films with the largest area were coated with a PVOH layer by solvent casting method (Fig. 1). A PVOH/water-based solution 1/4 wt content was used to coat the surfaces with the aim of avoiding the appearance of the non-foamed dense skins in those borders during the foaming.

On the other hand, the porous membranes were produced by gas dissolution foaming using a high-pressure vessel (model PARR 4760) provided by Parr Instrument Company (Moline, IL, USA). Saturation conditions were fixed at 30 MPa and 40 °C and PMMA/MAM films were foamed in one-step foaming process. Thus, the gas barrier approach applied to gas dissolution foaming has allowed producing porous membranes with none, one, or two dense skins (Table 2) (labelled as '+0PVOH', '+1PVOH', and '+2PVOH' depending on the number of the gas diffusion barriers applied). More details about the use of the PVOH technique in gas dissolution foaming can be found elsewhere [34]. It is important to point out that PVOH layers have been removed after the foaming process and prior any characterization by employing an ultrasonic water bath.

Table 1
PMMA/MAM formulations for producing solid films.

PMMA/MAM	Content (wt%)	Solid density (g/cm^3)	Thickness (μm)
VT/M42 film	15/85	1.096	421 ± 25
8N/M53 film	15/85	1.156	381 ± 19

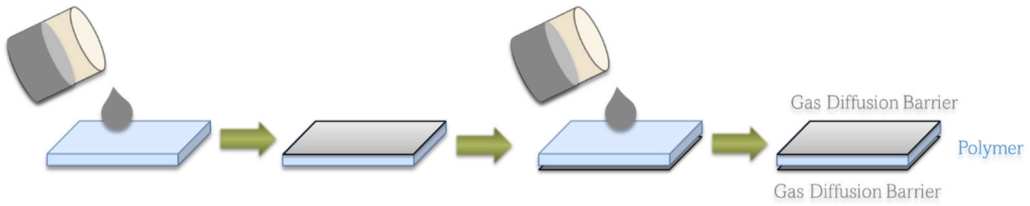

Fig. 1. Scheme of the methodology for incorporating the gas diffusion barrier to both top and bottom sides of the polymer. PMMA/MAM films are represented in blue while the PVOH incorporation (in grey) was made over each surface separately.

Table 2
PMMA/MAM porous membranes fabricated in this work.

Name	Gas barrier approach	Thickness (μm)
VT/M42 + 0PVOH	No	671 ± 60
VT/M42 + 1PVOH	One side	1182 ± 77
VT/M42 + 2PVOH	Two sides	1010 ± 82
8N/M53 + 0PVOH	No	603 ± 47
8N/M53 + 1PVOH	One side	820 ± 71
8N/M53 + 2PVOH	Two sides	981 ± 78

2.3. Characterization techniques

2.3.1. Solid and foam densities

Density of the solid samples was measured with a gas pycnometer (Mod. AccuPyc II 1340, Micromeritics, Norcross, GA, USA). Foams density was measured using the water-displacement method based on Archimedes' principle, employing a density determination kit for an AT261 Mettler-Toledo balance (Columbus, OH, USA). Relative density has been calculated from the relationship between the foam density and the solid density.

2.3.2. Cellular structure

Cellular structure of PMMA/MAM membranes (cell density (N_v) and cell size (Φ)) was analyzed from micrographs by Scanning Electron Microscopy (SEM) using a Merlin SEM (Zeiss, Germany). The SEM was operated at an accelerating voltage of 1.5 kV and a probe current of 35 pA, using a high efficiency Everhart-Thornley (HE-S2) and an InLens secondary electron detector. First, samples were cooled in liquid nitrogen and then fractured to expose the inner cellular structure without damage. Before the measurement, the specimens were dried in vacuum and the surfaces to visualize (both cross-section and external surfaces achieved in samples with or without PVOH barrier) were sputter-coated with 1.5 nm platinum using a CCU-010 coating device (Safematic, Switzerland). Cross-section SEM micrographs were used in combination with a specific software based on ImageJ/FIJI for the detailed characterization of the cellular structure [41]. First, cell density (N_v) in three dimensions was calculated using Kumar's theoretical approximation [42] according to Eq. 1.

$$N_v = \left(\frac{n}{A}\right)^{\frac{3}{2}} \quad (1)$$

Where N_v is the cell density (3D), n is the number of cells, and A is the analyzed area. On the other hand, cell size (Φ) was calculated as the average value of the cell diameter measurements from SEM micrographs in two different regions for at least 50 cells in each [41].

2.3.3. Dense skins thickness

The dense skin thickness (l) was directly measured from the cross-section SEM micrographs employing ImageJ/FIJI software [43] according to a procedure previously published [34]. The average thickness of non-foamed skins for each top and bottom surfaces are provided in this work. Fig. 2 shows an example of the methodology followed for measuring the dense skin thicknesses.

2.3.4. Membrane thickness

The thickness of the films and the porous membranes were given by the average of the thickness measurements by a thickness measuring instrument (Dualscope® MP0R from Fischer) by taking at least 40 measurements of the thickness per sample.

2.3.5. Time-lag measurements

Gas permeability measurements were performed by a constant-volume gas permeator device based on the time-lag methodology [44, 45]. More details about time-lag measurements device are provided in the Supporting Information *(Section S2)*.

For time-lag measurements, films and porous membranes were cut in

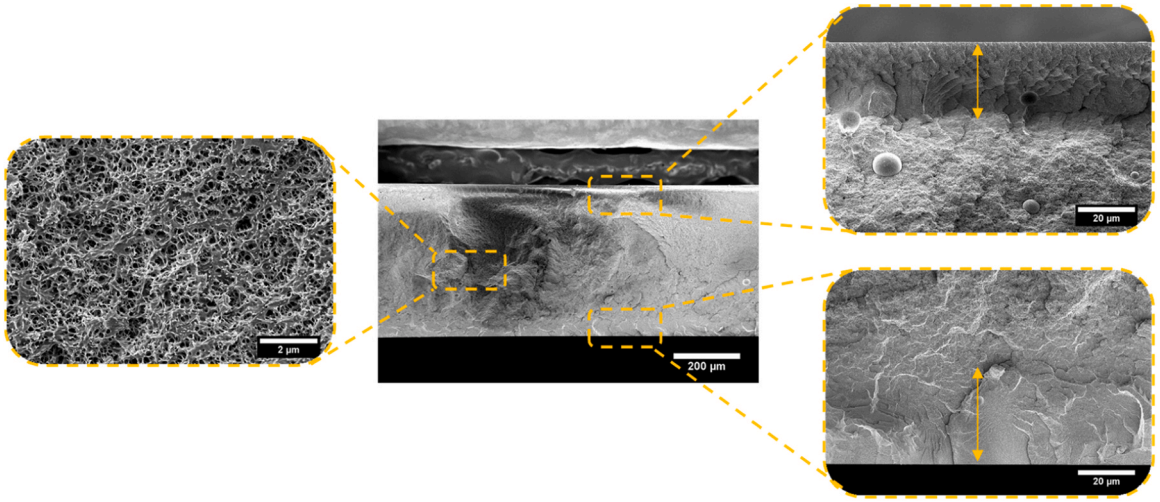

Fig. 2. Example of SEM micrographs from a porous membrane with dense skins in the borders and a foamed core. Micrographs correspond to VT/M42 membrane.

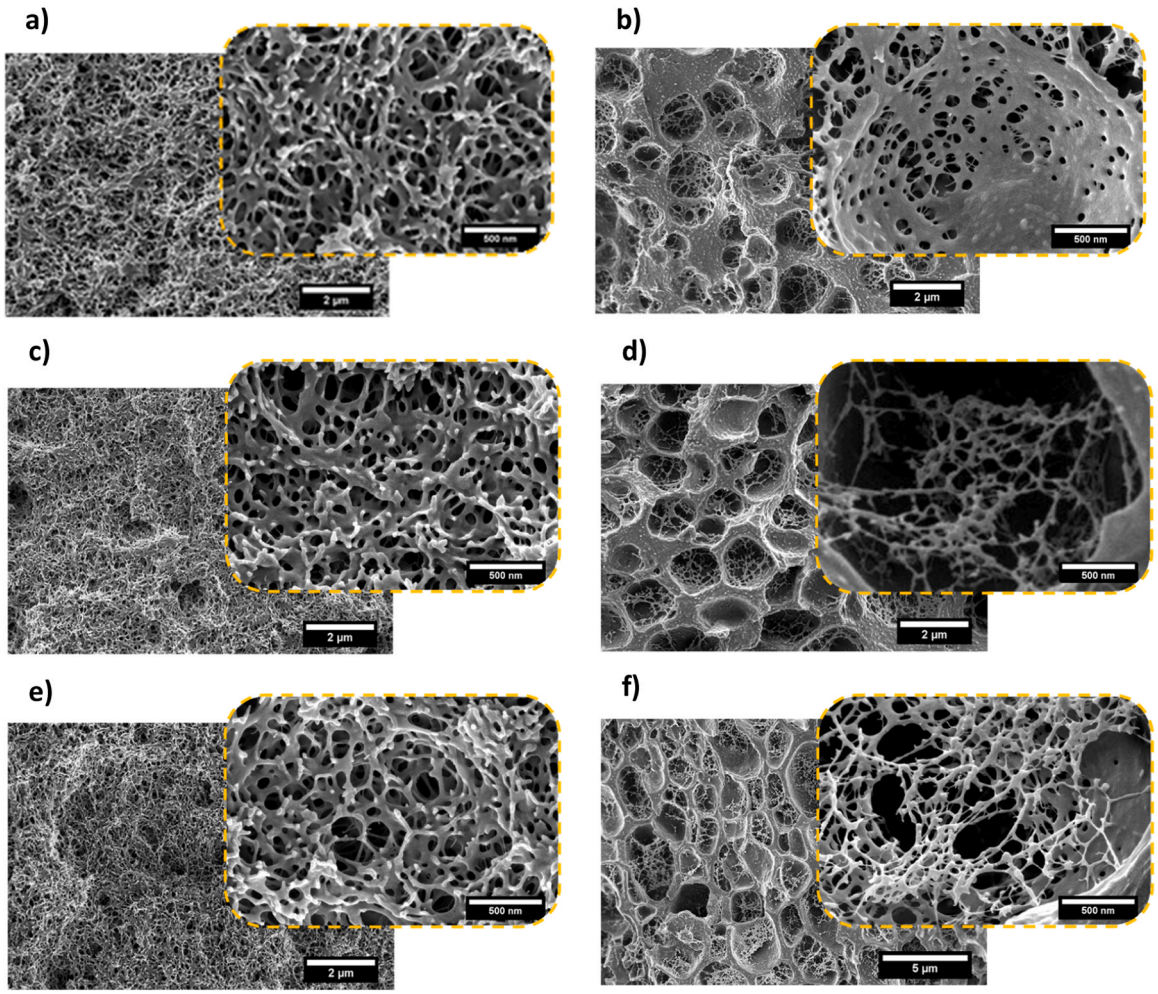

Fig. 3. SEM micrographs of VT/M42 and 8N/M53 formulations. **a)** VT/M42 + 0PVOH, **b)** 8N/M53 + 0PVOH, **c)** VT/M42 + 1PVOH, **d)** 8N/M53 + 1PVOH, **e)** VT/M42 + 2PVOH, and **f)** 8N/M53 + 2PVOH.

circles (2.5 cm of diameter) for being coupled in the permeation cell. However, the effective area of the gas flux through the membrane was 2.2 cm^2. First, the gas permeator was maintained under vacuum during 24 h for ensuring the total evacuation of the air inside itself and also in the membrane. Then, gas permeability measurements were carried out at a constant pressure and temperature (3 bar and 35 °C) for helium, nitrogen, oxygen, methane, and carbon dioxide.

Gas permeability coefficient (P) is calculated from the flow rate in the downstream (Eq. 2), expressed in Barrers (Ba) [1 Barrer $= 10^{-10}$ (cm^3 (STP)·cm) / (cm^2·s·cmHg)].

$$P = \frac{273}{76} \cdot \frac{V}{A} \frac{l}{T} \frac{}{p_0} \cdot \frac{dp}{dt} \tag{2}$$

Where V is the volume of the low-pressure side, A is the effective area of the membrane, p_0 is the pressure of the high-pressure side, T is the temperature, and dp/dt is referred to the pressure variation as a function of the time in the downstream side. Besides, the selectivity (α) for a pair of gases and the permeance (G) were calculated from Eq. 3 and Eq. 4, respectively. Where the ideal selectivity for a pair of gases is defined as the permeability ratio between the faster permeating gas (P_a), and the slower permeating gas, (P_b). The permeance (G) is expressed in Gas Permeation Units, [1 GPU $= 10^{-6}$ (cm^3 (STP)) / (cm^2·s·cmHg)] [11].

$$\alpha_{a/b} = \frac{P_a}{P_b} \tag{3}$$

$$Permeance(GPU) = \frac{P(Ba)}{l(\mu m)} \tag{4}$$

Table 3
Relative density, cell density, and cell size of the PMMA/MAM membranes (VT/M42 and 8N/M53) without PVOH on the surfaces (+0PVOH), with PVOH on one surface (+1PVOH), and with PVOH on two surfaces (+2PVOH).

Name	Relative density	Cell density (cell/cm^3)	Cell size (nm)
VT/M42 + 0PVOH	0.816 ± 0.002	(1.75 ± 0.21)·10^{13}	131 ± 48
VT/M42 + 1PVOH	0.765 ± 0.001	(2.19 ± 0.28)·10^{13}	123 ± 35
VT/M42 + 2PVOH	0.737 ± 0.002	(2.78 ± 0.33)·10^{13}	130 ± 46
8N/M53 + 0PVOH	0.571 ± 0.001	(6.24 ± 0.53)·10^{11}	1110 ± 330
8N/M53 + 1PVOH	0.479 ± 0.001	(5.70 ± 0.42)·10^{11}	1340 ± 344
8N/M53 + 2PVOH	0.387 ± 0.001	(1.66 ± 0.59)·10^{11}	1880 ± 594

Table 4
Results of the top and bottom dense skin thickness of PMMA/MAM porous membranes. In '+ 1PVOH' membranes the PVOH was located on the bottom surface. Cell size of the top and bottom surfaces is also displayed.

Name	Top dense layer (μm)	Bottom dense layer (μm)	Cell size (μm). Top surface	Cell size (μm). Bottom surface
VT/M42 + 0PVOH	26.0 ± 4.2	30.6 ± 7.1	-	-
VT/M42 + 1PVOH	25.7 ± 5.6	2.1 ± 0.4	-	2.3 ± 1.1
VT/M42 + 2PVOH	1.3 ± 0.3	1.7 ± 0.3	1.2 ± 0.9	2.5 ± 1.2
8N/M53 + 0PVOH	52.9 ± 1.4	60.0 ± 4.7	-	-
8N/M53 + 1PVOH	39.8 ± 4.2	3.9 ± 1.7	-	1.2 ± 0.4
8N/M53 + 2PVOH	3.8 ± 2.0	2.1 ± 1.5	1.0 ± 0.5	0.9 ± 0.4

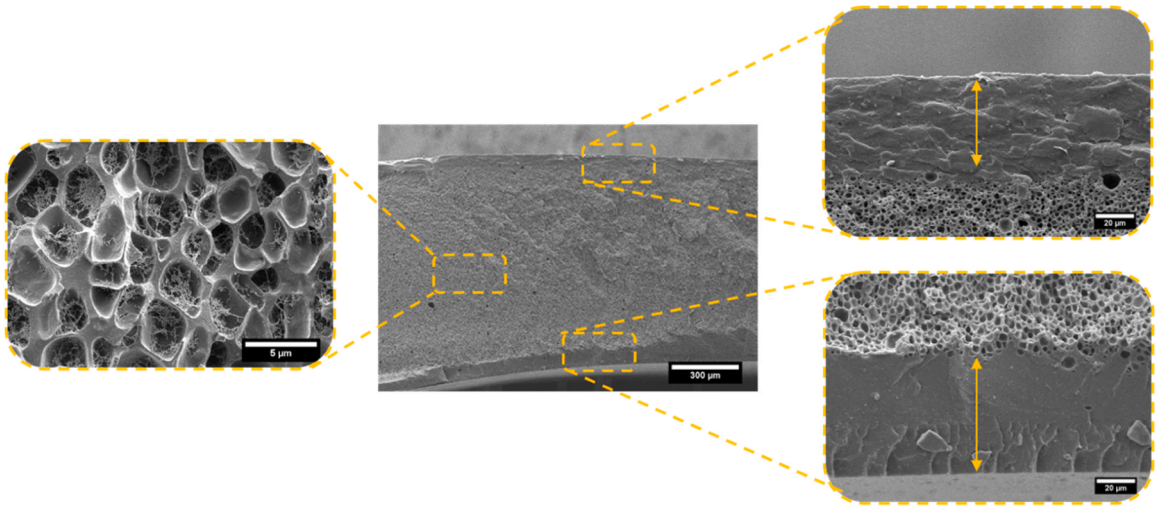

Fig. 4. Morphology of the 8N/M53 membrane along the thickness: homogeneous cellular structure in the centre and dense layer in the edges.

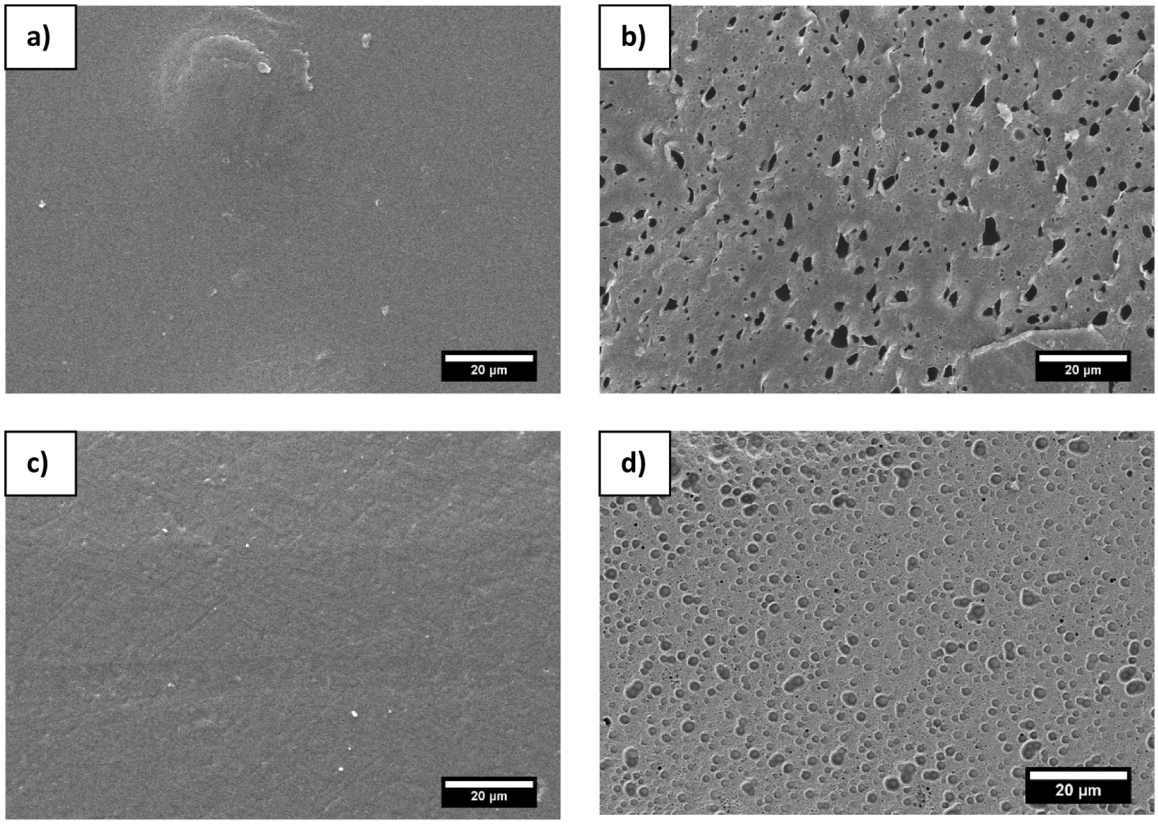

Fig. 5. Comparison of the surface morphology between porous membranes fabricated with and without using the gas diffusion barrier. **a)** VT/M42 + 0PVOH, **b)** VT/M42 + 2PVOH, **c)** 8N/M53 + 0PVOH, and **d)** 8N/M53 + 2PVOH.

3. Results

3.1. Cellular structure

The cellular structure of the produced PMMA/MAM membranes has been analyzed from the SEM micrographs. Fig. 3 shows the cellular structure of VT/M42 and 8N/M53 formulations by employing or not the gas barrier approach. Besides, the relative density, the cell density, and the cell size according to those SEM micrographs are displayed in Table 3.

VT/M42 membranes present a homogenous open-cell nanocellular structure (Fig. 3a, c, and e) with cell densities over 10^{13} cells/cm^3 and cell sizes around 130 nm (Table 3). It is important to point out that cell density in open-cell foams is a parameter quite inaccurate since the morphology of one cell is clearly undefined due to its interconnection to each other. Therefore, slight changes are obtained in cell density (N_v) while the relative density decreases in VT/M42 + 1PVOH and VT/M42 + 2PVOH due to the whole foaming reached in the edges. The formation of an homogeneous porous structure till the edges of the film is promoted by a gas concentration increment in the edges allowing the foaming also in these regions and obtaining samples with larger expansion [34].

On the other hand, a complex cellular structure was obtained in 8N/M53 formulations: an open-cell nanocellular structure (not taken into account in N_v) was formed inside of the micropores which build a mesostructured (Fig. 3b, d, and f), apparently close-cell, presenting lower cell densities than VT/M42 membranes (around 10^{11} cells/cm^3) and larger cell sizes (around 1–2 μm). Recently, Demewoz et al. [46] obtained similar bimodal structures from PMMA/TPU blends, affirming that the 'bouquet-like structure' was formed by a combination of spinodal decomposition from PMMA-CO_2 and nucleation from TPU particles [47,48]. However, the differences between the cellular structures obtained in this work (Fig. 3) are more related to the physical properties of the MAM phase, as it was proved in a previous work [40]. MAM M53 presents higher viscoelastic properties that are associated to higher PBA contents (the soft phase of MAM) allowing higher expansion ratios while M42 shows more rigidity in the cell growth. For supporting that discussion, similar open-cell nanocellular structures were achieved for M42 and M53 blends at lower temperature (30 °C), demonstrating that the rheologic properties as a function of the saturation temperature has a decisive impact on the cell growth [40]. In this way, Pinto et al. [49] attributed the relative density and cell density reductions to cell coalescence promoted by raising the saturation temperature in PMMA/-MAM blends. To sum up, open-cell nanocellular structures and bimodal (open-cell nanocellular and close-cell mesoporous) structures were produced in all the situations (none, one, or two dense layers). More discussion about the morphology of the cellular structure in PMMA/-MAM blends can be found elsewhere [40].

3.2. Dense skin layers thickness

The use of the gas barrier approach on the polymer films determinates the appearance of the dense skin layers. The thicknesses of the dense skin layers of the PMMA/MAM membranes are displayed in Table 4.

In VT/M42 membranes the typical dense skin thicknesses without using the gas barrier approach are in the range between 25 and 30 μm in each side (Fig. 2, Table 4). On the contrary, the thickness of the dense layer was successfully reduced until 1 μm in the side whereby the gas diffusion barrier was applied. Similarly, dense skins in 8N/M53 + 0PVOH membrane resulted above 50 μm (Fig. 4, Table 4) while the thickness was again reduced to 2 μm by employing the gas diffusion barrier on those surfaces (8N/M53 +1PVOH and 8N/M53 +2PVOH). The differences between M42 and M53 blends could be related to their viscoelastic properties. M42 presented a harder rigid behavior which would allow retain the gas easier than M53, leaving lower dense skin thicknesses [40].

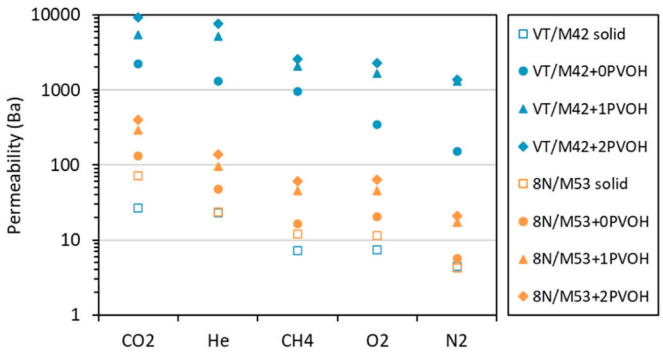

Fig. 6. Permeability of the VT/M42 (blue symbols) and 8N/M53 (orange symbols) membranes for CO_2, He, CH_4, O_2, and N_2.

Moreover, the analysis of the surface morphology aroused that a porous distribution was obtained on the surfaces which were coated with the gas diffusion barrier, while smooth solid surfaces were found in the others (Fig. 5). The gas diffusion barrier not only promotes an increase of the CO_2 gas concentration next to the edges of the films, but the accumulation of the gas molecules in the polymer-PVOH interface allows creating pores on the surfaces by heterogeneous nucleation [34]. The average diameter of the pores is around 1–2 μm, quite similar to the dense skin thicknesses previously measured (Table 4). Thus, we can assume that dense skins were completely removed (i.e., thicknesses in the same order of magnitude of the pores distributed along this layer) from those borders whereby the gas diffusion barrier was employed. Therefore, the gas dissolution foaming in combination to the gas barrier approach allows to achieve open porous membranes with full control on the formation of dense layers in the edges. More detailed SEM micrographs regarding the cellular structure near the edges and the dense layers are included in the Supporting Information (Section S3).

3.3. Time-lag

Taking advantage of the cellular structures created from VT/M42 and 8N/M53 formulations, the permeability and selectivity, the permeance, and the effect of the dense skins as selective layers were analysed from time-lag measurements.

3.3.1. Permeability and selectivity

The gas separation performances offer an idea of the applicability of a membrane in a specific gas separation application. Fig. 6 shows the permeability of membranes derived from VT/M42 and 8N/M53 blends (results are listed in Table 5). First, comparing the solid polymer films (void squares), similar permeabilities were obtained for both PMMA/MAM compositions, being those of 8N/M53 a little bit higher than the obtained for VT/M42.

Comparing permeabilities between different gases, both PMMA and MAM present a very high CO_2 affinity which explains the highest values in permeability in both VT/M42 and 8N/M53 films. Second, the

Table 5
Permeability of all membranes for all gases: CO_2, He, CH_4, O_2, and N_2. Unit conversion: 1 Ba = $3.35{\cdot}10^{-16}$ [mol·m·s^{-1} ·m^{-2} ·Pa^{-1}].

Name	P_{CO2} (Ba)	P_{He} (Ba)	P_{CH4} (Ba)	P_{O2} (Ba)	P_{N2} (Ba)
VT/M42 film	27	23	7	7	4
VT/M42 + 0PVOH	2201	1302	954	345	150
VT/M42 + 1PVOH	5400	5246	2059	1662	1308
VT/M42 + 2PVOH	9368	7707	2570	2268	1386
8N/M53 film	72	24	12	11	4
8N/M53 + 0PVOH	132	50	17	20	6
8N/M53 + 1PVOH	290	96	45	45	17
8N/M53 + 2PVOH	404	139	61	64	21

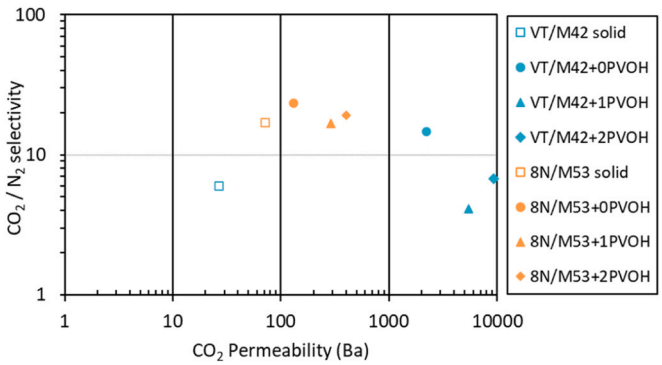

Fig. 7. CO_2/N_2 selectivity as a function of the CO_2 permeability for all membranes.

Table 6
Selectivity of O_2/N_2, CO_2/CH_4, and CO_2/N_2.

Name	$\alpha_{O2/N2}$	$\alpha_{CO2/CH4}$	$\alpha_{CO2/N2}$
VT/M42 film	1.6	3.7	6.0
8N/M53 film	2.7	6.0	17.0

permeability values follow the kinetic diameter for helium, oxygen, and nitrogen. However, methane surprisingly shows higher values than expected according to its kinetic diameter. This is probably explained due to a combined effect of a specific interaction and an increase in solubility of CH_4 in the soft segregated domains of the copolymer [50]. This permeability trend is also observed in the porous membranes. This indicates that the films and the dense skins of the foamed films are similar or dominant on the separation performances.

As expected, the permeability of porous membranes increased significantly due to the creation of the cellular structure, existing several differences between both formulations. It is clear that the open-cell structures showed by VT/M42 porous membranes (Fig. 3a, c, and e) allow reaching higher increments in permeability than the close-cell mesoporous structures presented by the 8N/M53 membranes (Fig. 3b, Fd, and f). Moreover, a further increase in permeability is reached by extending the foaming to the edges, reaching 333 and 5.5 times of enhancement in VT/M42 + 2PVOH and 8N/M53 + 2PVOH with respect to corresponding solid film. Therefore, it seems that the dense layers are acting as selective layers while the cellular structure serves as a support with strong mechanical properties as it has been proven in nanocellular polymers [51,52].

According to the selectivity/permeability plot (Fig. 7), the selectivity of a pair of gases depends on the PMMA/MAM formulation used while the permeability increased with the porosity of the membrane. In addition, it seems that the PMMA/MAM blends selected for this work

Table 7
Permeances of all membranes for all gases: CO_2, He, CH_4, O_2, and N_2. Unit conversion: 1 GPU = $3.35{\cdot}10^{-10}$ [$mol{\cdot}s^{-1}{\cdot}m^{-2}{\cdot}Pa^{-1}$].

Name	P_{CO2} (GPU)	P_{He} (GPU)	P_{CH4} (GPU)	P_{O2} (GPU)	P_{N2} (GPU)
VT/M42 film	0.054	0.064	0.011	0.017	0.017
VT/M42 + 0PVOH	1.940	3.282	0.224	1.423	0.514
VT/M42 + 1PVOH	4.438	4.569	1.107	1.742	1.406
VT/M42 + 2PVOH	7.631	9.276	1.373	2.544	2.246
8N/M53 film	0.011	0.063	0.188	0.030	0.031
8N/M53 + 0PVOH	0.011	0.096	0.264	0.041	0.033
8N/M53 + 1PVOH	0.021	0.117	0.353	0.055	0.055
8N/M53 + 2PVOH	0.022	0.142	0.412	0.065	0.062

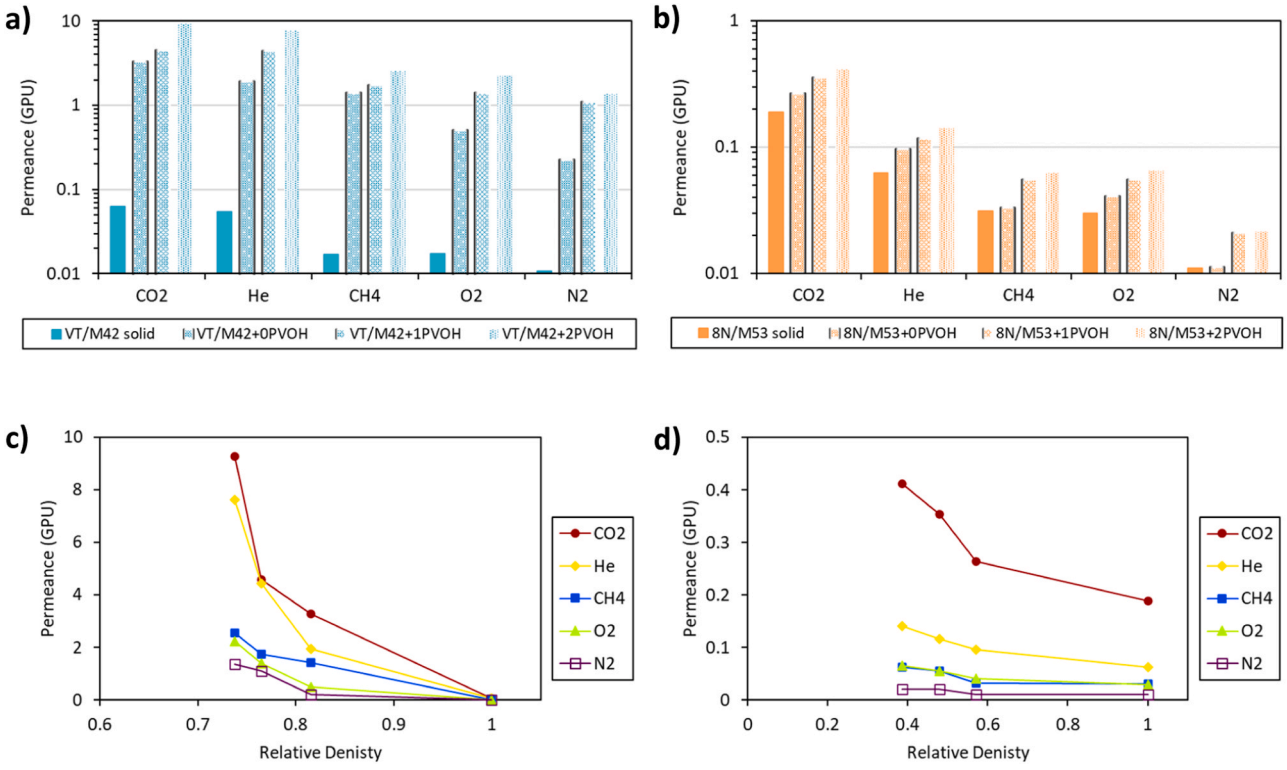

Fig. 8. Permeance of the **a)** VT/M42 (in blue) and **b)** 8N/M53 (in orange) membranes for different gases: CO_2, He, CH_4, O_2, and N_2. Permeance as a function of the relative density for **c)** VT/M42 and **d)** 8N/M53 membranes for different gases: CO_2, He, CH_4, O_2, and N_2.

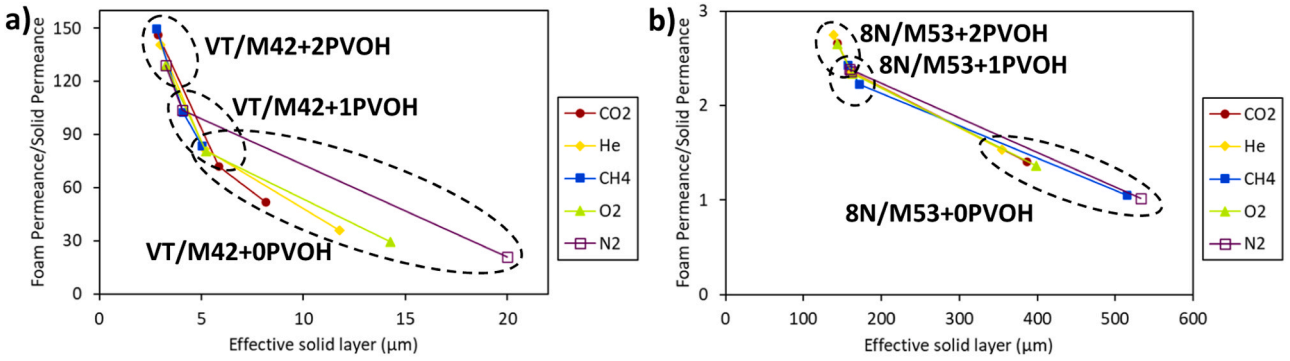

Fig. 9. Relative permeance as a function of the thickness related to effective dense layer of the **a)** VT/M42 and **b)** 8N/M53 membranes for different gases: He, N_2, O_2, CH_4, and CO_2. Black dotted circles.

would present the most appropriate behavior in gas separation for the CO_2/N_2 pair of gases since that selectivity reached the highest values (Table 6). However, the objective of this work is to proof the concept of formation of a porous structure membrane with a defect-free thin dense layer on top by a solvent-free method. A comparison of the gas permeability and selectivity data is included in the Supporting Information (Section S4).

3.3.2. *Permeance*

The permeance or gas flux is more accurate once the membranes are formed by thin selective layers. Permeance gives a better overview of the capacity of a membrane to be employed in an industrial gas separation process, [11]. In order to prove the strength of inducing a cellular structure over the gas flux in gas separation membranes, the permeance of the VT/M42 and 8N/M53 membranes is analyzed in this section (Fig. 8 and Table 7). As expected, both VT/M42 (Fig. 8) and 8N/M53 (Fig. 8**b**) porous membranes showed a permeance increase with respect to the thick films, following the same trend as in permeability regardless the gas employed. In addition, the reduction on the relative density, due to the elimination of the dense layer in the edges, allowed reaching significant increments in permeance (Fig. 8c and d). Therefore, gas dissolution foaming in combination with the gas barrier technique has been validated as an excellent method to form an asymmetric membrane in a single step with a solvent-free process. On the other hand, avoiding the formation of dense layers in the edges (membranes +1PVOH, and +2PVOH) seems to work better in the case of the VT/M42 than for 8N/M53, where the permeance for all the gases showed a lower increase (Fig. 8d). Probably, the effect is due to the thicker and close-cell walls presented by the 8N/M53 porous membranes, hampering the gas flux through close-cell structures (Fig. 3b, d, and f). Therefore, the permeance is controlled by the amount of porosity created in the gas dissolution foaming process while the selectivity will be determined by the intrinsic selectivity of the materials, MAM as a major phase in this case.

3.3.3. *Effective thickness of the dense layer*

Effectively, the gas permeance is a contribution of the dense layer and the resistance of the porous support. Therefore, the gas flux can be controlled by controlling the cellular structure of the membranes, i.e., by modifying the porosity, the cell interconnection (open-cell or close-cell) and the thickness of the selective layer. These kind of structures works as an electric circuit where the gas flux would be the intensity and the solid barriers (dense layers and cell walls) operates as the resistances [4]. However, the information about the real thickness of the dense layer (i.e., the total resistance of the circuit) cannot be directly provided. In order to calculate the resistance, the thickness of the effective dense layer (l_{eff}) in porous membranes was calculated from the relationship between the foam permeance and the solid film permeability (Eq. 5).

$$l_{eff} = \frac{P_{solid}(Ba)}{\frac{P_{foam}(Ba)}{l\ (\mu m)}} = \frac{Permeability_{solid}}{Permeance_{foam}} \quad (5)$$

Assuming the foamed sample will provide the same separation performances than the thick film, the differences in the gas flows must be due to the resistance of the dense layers and the porous substrate. Then, the permeance of the porous membranes normalized by the permeance of the films was plotted against the thickness of the effective dense layer for each gas measured (Fig. 9).

First, the permeance of porous membranes with regard to the permeance of the films increased significantly, reaching values up to 150 times of permeance enhancement for VT/M42 + 2PVOH membrane. Second, the effective dense layer was reduced when the dense layers are eliminated from the edges, as expected. In the VT/M42 + 2PVOH case, the effective dense layer, which is around 3 μm for all gases (Fig. 9a), which is in concordance with the measured dense layer thickness observed by SEM (Table 4). Thus, a total interconnection between cells can be assumed, confirming the open-cell structures seen in SEM micrographs (Fig. 3e). In this case, it can be assumed that the gas separation is dominated by the dense layer and the porous substrate does not offer any resistance to the gas flux. However, in porous membranes with

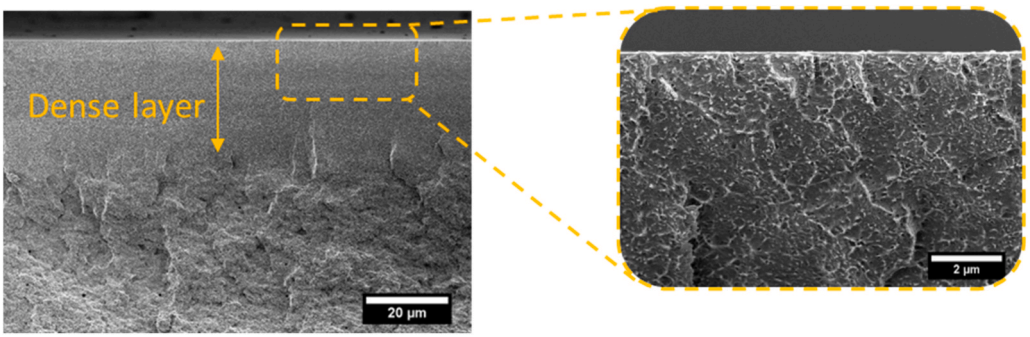

Fig. 10. SEM micrograph from the border of VT/M42 + 0PVOH. Also, high magnification micrograph of the dense layer is provided.

dense layers in the edges (VT/M42 +1PVOH and VT/M42 +0PVOH), where the PVOH gas barrier was not applied or only applied in one of the sides, the measured thickness of the dense skins (Table 4) resulted higher than the effective dense layer, showing less solid resistance than expected. In these cases, not only assuming that open cells are obtained but some porosity was found in the dense layer region (Fig. 10), promoting an underrated value of the effective dense layer.

On the other hand, the effective gas flow resistance for 8N/M53 porous membranes resulted much higher than the measured thickness of the dense layer, showing values for the sample 8N/M53 + 0PVOH between 350 and 36 μm (Fig. 9b) while the dense layer thickness measured was around 60 μm in each border (Table 4). As it was commented before, the solid resistance in this case is composed of dense skins in the borders and cell walls of the close-cell structure (Fig. 3b, d, and f). Moreover, assuming that 8N/M53 + 2PVOH presented no densified areas close to the edges of the membrane (around 1 μm, Table 4) the effective dense layer would correspond to the resistance showed by the cell walls, around 350 μm in the best case. Consequently, the thickness of the close-cell walls is contributing to the resistance for the gas flux, i.e., promoting an increase of the effective dense layer with respect to open-cell structures.

4. Conclusions

A new solvent-free methodology for processing a material into a gas separation membrane is presented in this work. Porous membranes with open-cell or close-cell structures were produced by CO_2 dissolution foaming from PMMA/MAM polymer blends. Besides, the gas barrier approach has been employed in the foaming process in order to obtain porous membranes with none, one, and two dense layers in the edges of the membranes. Thus, the relative density of the membranes was reduced and controlled from the thickness of the dense layers and the porosity induced on the surfaces by the same process.

The separation performances of the membranes were analyzed from a time-lag device and correlated to the cellular structures. In general, the selectivity depends on the polymer employed while permeability was tuned from the cell morphology. Open-cell structures showed a significant increase in permeability properties while close-cell structures presented strong resistance to the gas flux. In addition, the reduction in the relative density associated to the removal of the dense layers in the edges lead to an additional increment in permeance. By merging open-cell structures and reducing the thickness of the dense layers, the effective dense layer was decreased till 2 μm in total membrane thicknesses around 1000 μm. Thus, this solvent-free foaming methodology allows the production of membranes presenting a high-porosity and low resistance porous support, with tunable thickness for the selective layer. Therefore, this methodology has been validated as a green technique for creating, in a single foaming step, an asymmetric membrane for gas separation with tunable selective layer thickness and an open-porous structure providing mechanical support, without compromising the membrane performances.

CRediT authorship contribution statement

D. Cuadra-Rodríguez: Conceptualization, Methodology, Investigation, Writing – original draft. **C. Soto:** Investigation, Writing – review & editing. **F.J. Carmona:** Writing – review & editing. **A. Tena:** Conceptualization, Methodology, Writing – review & editing. **L. Palacio:** Writing – review & editing, Funding acquisition. **M. A. Rodríguez-Pérez:** Supervision, Funding acquisition. **J. Pinto:** Conceptualization, Writing – review & editing, Supervision.

Declaration of Competing Interest

The authors declare that they have no known competing financial interests or personal relationships that could have appeared to influence the work reported in this paper.

Data Availability

No data was used for the research described in the article.

Acknowledgements

Financial assistance from Ministerio de Ciencia e Innovación (Spain) (PRE2019-088820), Ministerio de Ciencia, Innovación y Universidades (MCIU) (Spain), MCIN/AEI /10.13039/501100011033 and the EU NextGenerationEU/ PRTR program (PLEC2021-007705), FEDER (EU) (RTI2018 - 098749-B-I00, RTI2018 - 097367-A-I00, PID2021-127108OB-I00, PID2019-109403RB-C21/AEI/10.13039/501100011033, TED2021-130965B-I00 and PDC2022-133391-I00), Regional Government of Castilla y León and the EU-FEDER program (CLU-2019-04 and VA202P20), are gratefully acknowledged. This work was supported by the Regional Government of Castilla y León (Junta de Castilla y León), and by the Ministry of Science and Innovation MICIN and the European Union NextGenerationEU/PRTR.

Appendix A. Supporting information

Supplementary data associated with this article can be found in the online version at doi:10.1016/j.jcou.2023.102536.

References

[1] T. Gerres, J.P. Chaves Ávila, P.L. Llamas, T.G. San Román, A review of cross-sector decarbonisation potentials in the European Energy Intensive Industry, J. Clean. Prod. 210 (2019) 585–601, https://doi.org/10.1016/j.jclepro.2018.11.036.
[2] Z. Dai, L. Ansaloni, L. Deng, Recent advances in multi-layer composite polymeric membranes for CO_2 separation: a review, Green. Energy Environ. 1 (2016) 102–128, https://doi.org/10.1016/J.GEE.2016.08.001.
[3] X.Q. Cheng, Z.X. Wang, X. Jiang, T. Li, C.H. Lau, Z. Guo, J. Ma, L. Shao, Towards sustainable ultrafast molecular-separation membranes: from conventional polymers to emerging materials, Prog. Mater. Sci. 92 (2018) 258–283, https://doi.org/10.1016/J.PMATSCI.2017.10.006.
[4] C.Z. Liang, T.S. Chung, J.Y. Lai, A review of polymeric composite membranes for gas separation and energy production, Prog. Polym. Sci. 97 (2019), 101141, https://doi.org/10.1016/j.progpolymsci.2019.06.001.
[5] J.K. Mitchell, On the penetrativeness of fluids, J. Memb. Sci. 100 (1995) 11–16, https://doi.org/10.1134/S0001434610110349.
[6] G. Maier, Gas separation with polymer membranes, *Angew.* Chemie Int. Ed (1998) 2960–2974.
[7] Scott, K.; Hughes, R. Industrial Membrane Separation Technology; Blackie Academic & Professional, 1996;
[8] K. Ghosal, B.D. Freeman, Gas separation using polymer membranes: an overview, Polym. Adv. Technol. 5 (1994) 673–697, https://doi.org/10.1002/PAT.1994.220051102.
[9] L. Zhao, E. Riensche, R. Menzer, L. Blum, D. Stolten, A parametric study of CO_2/N2 gas separation membrane processes for post-combustion capture, J. Memb. Sci. 325 (2008) 284–294, https://doi.org/10.1016/J.MEMSCI.2008.07.058.
[10] L.M. Robeson, Correlation of Separation Factor versus Permeability for Polymeric Membranes, J. Memb. Sci. 62 (1991) 165–185, https://doi.org/10.1016/0376-7388(91)80060-J.
[11] K. Xie, Q. Fu, G.G. Qiao, P.A. Webley, Recent progress on fabrication methods of polymeric thin film gas separation membranes for CO_2 capture, J. Memb. Sci. 572 (2019) 38–60, https://doi.org/10.1016/J.MEMSCI.2018.10.049.
[12] Q. Fu, J. Kim, P.A. Gurr, J.M.P. Scofield, S.E. Kentish, G.G. Qiao, A novel cross-linked nano-coating for carbon dioxide capture † broader context, Energy Environ. Sci. 9 (2016) 434, https://doi.org/10.1039/c5ee02433a.
[13] A. Arabi Shamsabadi, M. Rezakazemi, F. Seidi, H. Riazi, T. Aminabhavi, M. Soroush, Next generation polymers of intrinsic microporosity with tunable moieties for ultrahigh permeation and precise molecular CO_2 separation, Prog. Energy Combust. Sci. 84 (2021), 100903, https://doi.org/10.1016/J.PECS.2021.100903.
[14] M. Wang, J. Zhao, X. Wang, A. Liu, K.K. Gleason, Recent progress on submicron gas-selective polymeric membranes, J. Mater. Chem. A (2017), https://doi.org/10.1039/c7ta01862b.
[15] J.M.S. Henis, M.K. Tripodi, The developing technology of gas separating membranes, Science 220 (1983) 11–17, https://doi.org/10.1126/science.220.4592.11.
[16] L. Xiang, Y. Pan, J. Jiang, Y. Chen, J. Chen, L. Zhang, C. Wang, Thin poly(Ether-Block-Amide)/attapulgite composite membranes with improved CO_2 permeance and selectivity for CO_2/N2 and CO_2/CH4, Chem. Eng. Sci. 160 (2017) 236–244, https://doi.org/10.1016/J.CES.2016.11.037.

[17] J. Peter, K.V. Peinemann, Multilayer composite membranes for gas separation based on crosslinked PTMSP gutter layer and partially crosslinked Matrimid® 5218 selective layer, J. Memb. Sci. 340 (2009) 62–72, https://doi.org/10.1016/J.MEMSCI.2009.05.009.
[18] P. Li, Z. Wang, W. Li, Y. Liu, J. Wang, S. Wang, High-performance multilayer composite membranes with mussel-inspired polydopamine as a versatile molecular bridge for CO_2 separation, ACS Appl. Mater. Interfaces (2015), https://doi.org/10.1021/acsami.5b03786.
[19] B. Wang, J. Xu, J. Wang, S. Zhao, X. Liu, Z. Wang, High-performance membrane with angstrom-scale manipulation of gas transport channels via polymeric decorated MOF cavities, J. Memb. Sci. (2021) *625*, https://doi.org/10.1016/J.MEMSCI.2021.119175.
[20] J. Liu, Xiandah, Ho, B. Park, H. Lin, High-performance polymers for membrane CO 2 /N 2 separation, Chem. Eur. J. 22 (2016) 15980–15990, https://doi.org/10.1002/chem.201603002.
[21] R. Ding, Y. Dai, W. Zheng, X. Li, X. Yan, Y. Liu, X. Ruan, S. Li, X. Yang, K. Yang, et al., Vesicles-shaped MOF-based mixed matrix membranes with intensified interfacial affinity and CO_2 transport freeway, Chem. Eng. J. 414 (2021), 128807, https://doi.org/10.1016/J.CEJ.2021.128807.
[22] C.S. Lee, M. Kang, K.C. Kim, J.H. Kim, In-Situ formation of asymmetric thin-film, mixed-matrix membranes with ZIF-8 in dual-functional imidazole-based comb copolymer for high-performance CO_2 capture, J. Memb. Sci. (2022) *642*, https://doi.org/10.1016/j.memsci.2021.119913.
[23] M.S. McCaig, D.R. Paul, Effect of film thickness on the changes in gas permeability of a glassy polyarylate due to physical AgingPart I. Experimental Observations, Polymers. 41 (2000) 629–637, https://doi.org/10.1016/S0032-3861(99)00172-X.
[24] J.M. Hutchinson, Physical aging of polymers, Prog. Polym. Sci. 20 (1995) 703–760, https://doi.org/10.1016/0079-6700(94)00001-I.
[25] Kratochvil, A.M. Thickness Dependent Physical Aging And Supercritical Carbon Dioxide Conditioning Effects On Crosslinkable Polyimide Membranes For Natural Gas Purification, Georgia Institute of Technology, 2008.
[26] Y. Huang, D.R. Paul, Physical aging of thin glassy polymer films monitored by gas permeability, Polymer 45 (2004) 8377–8393, https://doi.org/10.1016/J.POLYMER.2004.10.019.
[27] S. Kumar, J.H. Cho, I. Moon, Ionic liquid-amine blends and CO_2BOLs: prospective solvents for natural gas sweetening and CO_2 capture technology—a review, Int. J. Greenh. Gas. Control 20 (2014) 87–116, https://doi.org/10.1016/J.IJGGC.2013.10.019.
[28] U.W.R. Siagian, A. Raksajati, N.F. Himma, K. Khoiruddin, I.G. Wenten, Membrane-based carbon capture technologies: membrane gas separation vs. membrane contactor, J. Nat. Gas. Sci. Eng. 67 (2019) 172–195, https://doi.org/10.1016/J.JNGSE.2019.04.008.
[29] Eaves, D. Handbook of Polymer Foams; Eaves, D., Ed.; Rapra Technology Limited, 2004; ISBN 1–85957-388–6.
[30] S. Costeux, CO_2-Blown Nanocellular Foams. J. Appl. Polym. Sci, 2014, p. *41293*, https://doi.org/10.1002/app.41293.
[31] V. Kumar, N.P. Suh, A process for making microcellular thermoplastic parts, Polym. Eng. Sci. 30 (1990) 1323–1329, https://doi.org/10.1002/pen.760302010.
[32] V. Kumar, J.E. Weller, A model for the unfoamed skin on microcellular foams, Polym. Eng. Sci. 34 (1994) 169–173, https://doi.org/10.1002/pen.760340302.
[33] J. Pinto, S. Pardo, E. Solorzano, M.A. Rodriguez-Perez, M. Dumon, J.A. De Saja, Solid skin characterization of PMMA/MAM foams fabricated by gas dissolution foaming over a range of pressures, Defect Diffus. Forum 326–328 (2012) 434–439, https://doi.org/10.4028/www.scientific.net/DDF.326-328.434.
[34] D. Cuadra-Rodríguez, S. Barroso-Solares, M.A. Rodríguez Pérez, J. Pinto, Production of cellular polymers without solid outer skins by gas dissolution foaming: a long-sought step towards new applications, Mater. Des. 217 (2022), 110648, https://doi.org/10.1016/j.matdes.2022.110648.
[35] S. Barroso-Solares, D. Cuadra-Rodriguez, M.L. Rodriguez-Mendez, M.A. Rodriguez-Perez, J. Pinto, A new generation of hollow polymeric microfibers produced by gas dissolution foaming, J. Mater. Chem. B 8 (2020) 8820–8829, https://doi.org/10.1039/d0tb01560a.
[36] J. Pinto, M. Dumon, M.A. Rodriguez-Perez, R. Garcia, C. Dietz, Block copolymers self-assembly allows obtaining tunable micro or nanoporous membranes or depth filters based on PMMA; fabrication method and nanostructures, J. Phys. Chem. C. 118 (2014) 4656–4663, https://doi.org/10.1021/jp409803u.
[37] J.S. Colton, N.P. Suh, The nucleation of microcellular thermoplastic foam with additives: Part II: experimetntal results and discussion, Polym. Eng. Sci. 27 (1987) 485–492, https://doi.org/10.1002/pen.760270702.
[38] D. Cuadra-Rodríguez, X.-L. Qi, S. Barroso-Solares, M.Á.R. Pérez, J. Pinto, Microcellular foams production from nanocomposites based on PS Using MOF nanoparticles with enhanced CO_2 properties as nucleating agent, J. Cell. Plast. (2022) *58*, https://doi.org/10.1177/0021955×221087599.
[39] C. Forest, P. Chaumont, P. Cassagnau, B. Swoboda, P. Sonntag, Polymer nano-foams for insulating applications prepared from CO_2 foaming, Prog. Polym. Sci. 41 (2015) 122–145, https://doi.org/10.1016/J.PROGPOLYMSCI.2014.07.001.
[40] D. Cuadra-Rodríguez, S. Barroso-Solares, E. Laguna-Gutiérrez, M.Á. Rodríguez-Pérez, J. Pinto, Opening pores and extending the application window: open-cell nanocellular foams, Macromol. Mater. Eng. (2023) *2300087*, https://doi.org/10.1002/MAME.202300087.
[41] J. Pinto, E. Solorzano, M. a Rodriguez-Perez, J. a de Saja, Characterization of the cellular structure based on user-interactive image analysis procedures, J. Cell. Plast. 49 (2013) 555–575, https://doi.org/10.1177/0021955×13503847.
[42] Kumar, V.; Suh, N.P. Process Synthesis for Manufacturing Microcellular Thermoplastic Parts: A Case Study in Axiomatic Design. 1988.
[43] M.D. Abràmoff, P.J. Magalhães, S.J. Ram, Image processing with ImageJ, Biophotonics Int 11 (2004) 36–41, https://doi.org/10.1201/9781420005615.ax4.
[44] Daynes, H.A. The Process of Diffusion through a Rubber Membrane. Proc. R. Soc. London. Ser. A, Contain. Pap. a Math. Phys. Character 1920, 97, 286–307, doi: 10.1098/rspa.1920.0034.
[45] J. Marchese, M. Anson, N.A. Ochoa, P. Prádanos, L. Palacio, A. Hernández, Morphology and structure of ABS membranes filled with two different activated carbons, Chem. Eng. Sci. 61 (2006) 5448–5454, https://doi.org/10.1016/j.ces.2006.04.013.
[46] N.M. Demewoz, S.K. Yeh, Fabrication and characterization of low-density nanocellular foam based on PMMA/TPU blends, Polym. (Guildf.) (2022) *240*, https://doi.org/10.1016/J.POLYMER.2021.124493.
[47] S.K. Yeh, Z.E. Liao, K.C. Wang, Y.T. Ho, V. Kurniawan, P.C. Tseng, T.W. Tseng, Effect of molecular weight to the structure of nanocellular foams: phase separation approach, Polymer 191 (2020), 122275, https://doi.org/10.1016/j.polymer.2020.122275.
[48] H. Guo, A. Nicolae, V. Kumar, Solid-state poly(Methyl Methacrylate) (PMMA) nanofoams. Part II: low-temperature solid-state process space using CO_2 and the resulting morphologies, Polymer 70 (2015) 231–241, https://doi.org/10.1016/J.POLYMER.2015.06.031.
[49] J. Pinto, J.A. Reglero-Ruiz, M. Dumon, M.A. Rodriguez-Perez, Temperature influence and CO_2 transport in foaming processes of poly(Methyl Methacrylate)-block copolymer nanocellular and microcellular foams, J. Supercrit. Fluids 94 (2014) 198–205, https://doi.org/10.1016/j.supflu.2014.07.021.
[50] A. Tena, A. Marcos-Fernández, A.E. Lozano, J.G. De La Campa, J. De Abajo, L. Palacio, P. Prádanos, A. Hernández, Thermally segregated copolymers with PPO blocks for nitrogen removal from natural gas, Ind. Eng. Chem. Res. 52 (2013) 4312–4322, https://doi.org/10.1021/IE303378K/SUPPL_FILE/IE303378K_SI_001.PDF.
[51] B. Notario, J. Pinto, M.A. Rodríguez-Pérez, Towards a new generation of polymeric foams: PMMA nanocellular foams with enhanced physical properties, Polymers 63 (2015) 116–126, https://doi.org/10.1016/j.polymer.2015.03.003.
[52] S.K. Yeh, Y.C. Liu, C.C. Chu, K.C. Chang, S.F. Wang, Mechanical properties of microcellular and nanocellular thermoplastic polyurethane nanocomposite foams created using supercritical carbon dioxide, Ind. Eng. Chem. Res. 56 (2017) 8499–8507, https://doi.org/10.1021/acs.iecr.7b00942.